1556

U.S. Geological Survey - National Earthquake Hazards Reduction Program
Grant no 07HQGR0062

Observational and Geodynamic Constraints on Active Deformation in the Southern Illinois Basin

Michael Hamburger, Gerald Galgana, Kaj Johnson, Gary Pavlis, and Kim Shoemaker
Department of Geological Sciences, Indiana University, Bloomington, IN 47405

Final Technical Report
January 1, 2007 – December 31, 2009

Summary

This project combines high-precision GPS geodetic measurements in the southern Illinois Basin with geodynamic modeling to help constrain processes of present-day strain and seismicity in the tectonically active northern periphery of the New Madrid seismic zone. The project centers on reoccupation of a 56-site GPS geodetic network in southern Illinois, Indiana, and western Kentucky, plus a densified network of 35 sites in the Fluorspar district of southern Illinois. Through NEHRP support, we have successfully completed repeat measurements of the 56-station regional network (in summer 2007) and the 35-station Fluorspar district (in summer 2008), providing a ten-year record of crustal deformation in the region. We have completed our geodetic analysis of these data, and have integrated our results with other regional GPS geodetic data, in order to provide revised estimates of tectonic strain in the region. We use these newly obtained GPS geodetic velocities to develop elastic block models for present-day deformation in the region. We have also developed new geodynamic models that relate deformation in the Wabash Valley seismic zone with time-varying stresses associated with the 1811-1812 earthquakes in the New Madrid seismic zone. Our modeling examines the effect of New Madrid earthquakes on the near- and far-field strain and seismicity rates in the region through the processes of instantaneous elastic deformation in the lithosphere and associated postseismic viscoelastic flow in the asthenosphere. Preliminary results indicate significant changes in strain and seismicity rates in the southern Illinois Basin for several hundred years following the New Madrid earthquakes. The project promises to provide a stronger geodynamic framework for assessing earthquake hazards in the Illinois Basin region and to identify connections between two of the midcontinent's major seismically active source regions.

Background & Tectonic Setting

The southern Illinois Basin (Figure 1) has become the focus of increasing scientific interest over the past several years. This development has been sparked by a number of important discoveries, including newly accumulating evidence for large, prehistoric earthquakes in the region [e.g., *Obermeier et al.,* 1991; *Munson et al.,* 1995], evidence for Cenozoic faulting [*Sexton et al.,* 1986; *McBride et al.,* 2002], the presence of large geophysical anomalies [*Braile et al.,* 1982; *Hildenbrand & Ravat,* 1997], and a significant concentration of seismicity in the Wabash Valley area [*Nuttli*, 1979; *Braile et al.,* 1982; *Bear et al.,* 1997a; *Pavlis et al.,* 2002]. *Nuttli* [1979] dubbed this area the "Wabash Valley Seismic Zone" for its proximity to the Wabash River valley, which forms the boundary between Illinois and Indiana. The Wabash Valley is also associated with a prominent sequence of faults cutting the sediments in the southern edge of the Illinois Basin [e.g., *Nelson & Lumm,* 1984]. The area is also in close proximity to a number of other major structural features associated with the Illinois Basin, including the east-trending

Cottage Grove-Rough Creek-Shawneetown fault system, the magmatic system of Hicks Dome and the Flourspar district, and the north-trending La Salle, Du Quoin, and Clay City fold systems [*Nelson*, 1991; *Kolata & Nelson*, 1991].

Braile et al. [1982] proposed that the WVSZ may represent a northeastern extension of the New Madrid seismic zone, suggesting that the basement beneath the Illinois Basin may be underlain by similar, rift-generated structures. These structures were presumed to be part of a regional system of failed rifts associated with late Precambrian breakup of the Laurentian craton [*Braile et al.*, 1986; *Kolata and Nelson*, 1991]. This hypothesis was further supported by seismic reflection data collected in the WVSZ by *Sexton et al.* [1986], who identified prominent rift-related structures in a downdropped "Grayville graben", adjacent to the Wabash Valley fault zone. *Bear et al.* [1997] confirmed the presence of a narrow, well defined graben associated with the fault system, and documented significant strike-slip displacements on the major faults bounding the graben. These structures appear to have developed during latest Precambrian-early Cambrian, but show signs of repeated reactivation through Phanerozoic time. Much of the structural development of these features in the Paleozoic section apparently took place in latest Pennsylvanian or Permian time, possibly associated with regional compression following the Ouachita and Appalachian orogenies [*Kolata & Nelson*, 1991]. Seismic reflection data, combined with gravity and magnetic field analysis [Bear et al., 1997] image faults that extend to depths in excess of 7 km—well into the crystalline basement, and perhaps to mid-crustal depths. Sharp geophysical gradients are observed across the Commerce geophysical lineament, a basement structure that trends oblique to the WVFS [*Hildenbrand & Ravat*, 1997; *Hildenbrand et al.*, 2002; *McBride et al.*, 2002].

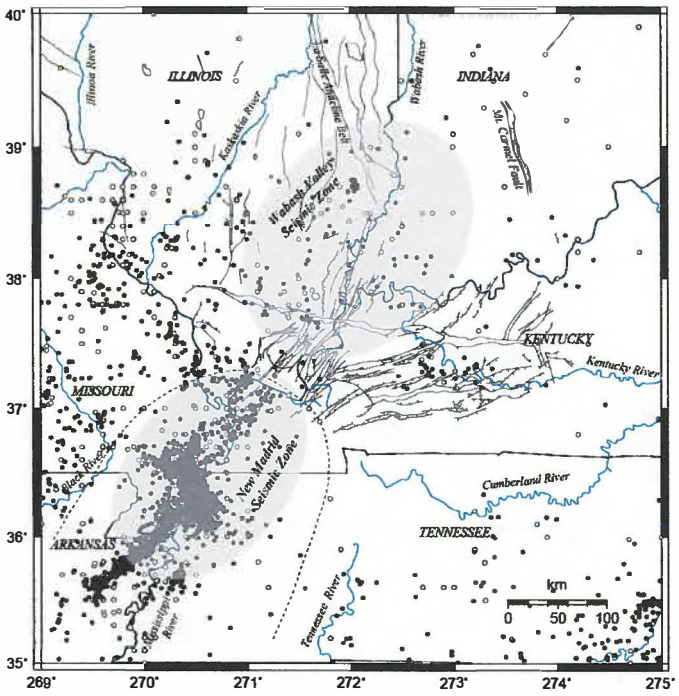

Figure 1: Seismotectonic setting of the Illinois Basin. Shaded ellipses show position of the New Madrid and Wabash Valley seismic zones. Open and filled circles indicate historical and instrumentally recorded earthquakes, respectively.

A number of sizeable earthquakes have occurred in the WVSZ in the past several years, including the m_b = 5.5 event of 9 November 1968 in southern Illinois [*Stauder and Nuttli*, 1970]; the m_b = 5.1 event of 10 June 1987 near the Illinois-Indiana border [*Taylor et al.*, 1989; *Hamburger & Rupp*, 1988]; and the m_b = 5.0 Evansville earthquake of June, 2002 [*Kim*, 2003]. The 2002 event is particularly significant, in that it demonstrated, for the first time, a direct correlation between an intraplate earthquake and a mapped fault (the Caborn Fault of the WVFS) [*Kim*, 2003]. The WVSZ also shows a concentration of microearthquake activity, as demonstrated by earthquake locations from our temporary seismic array deployment in WVSZ [*Pavlis et al.*, 2002; *Eagar et al.*, 2006].

GPS Geodetic Measurements

Our work builds on previous observations (made in 1997, 1998, and 2002) of a geodetic network in the southern Illinois Basin (Figure 2). The network consists of 56 geodetic sites in southern Indiana (20 sites), southern Illinois (23 sites), and western Kentucky (13 sites). The network includes 28 existing geodetic sites that are part of the National Geodetic Survey (NGS) network of first-order triangulation and/or leveling benchmarks, plus 25 newly installed bedrock benchmarks. A number of our sites overlapped with existing networks, including three sites in the NWU/JPL network in southern Illinois and western Kentucky, and 18 sites that are part of the B-order HARN (High Accuracy Reference Network) geodetic networks in Illinois, Kentucky, and Indiana. The measurements are also tied to continuous GPS sites in the region, including those operated by the U.S. Army Corps of Engineers in Memphis (MEM2) and St. Louis (STL2). Further details on the network observations can be found at *http://erp-web.er.usgs.gov/reports/ VOL40/cu/g3039.htm.* We also compare are results with those collected by two other groups working in the region: (1) a sparse, regional network, distributed across the region surrounding the NMSZ, deployed by a Northwestern University team [Weber et al., 1997; Newman et al., 1999], and (2) a continuous network in the New Madrid zone operated by the CERI group [Smalley et al., 2005].

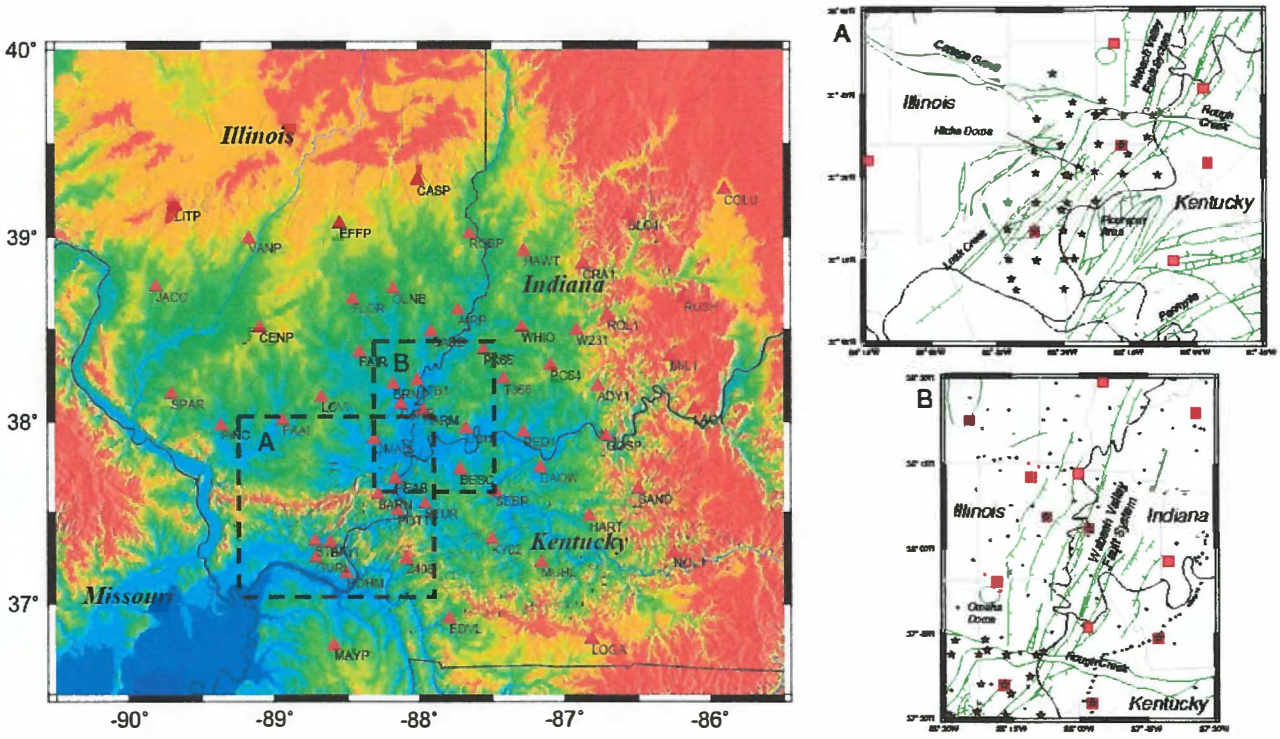

Figure 2: Southern Illinois Basin GPS network. Grey lines show mapped faults (assembled by Bear, 1997). Rectangles indicate areas of proposed densification, shown in insets A and B at right. (A) existing Shawnee Forest USFS network; (B) possible sites in WVFS area. Regional GPS network sites, other GPS benchmarks, and first-order leveling or triangulation sites are shown by squares, stars, and circles, respectively.

Field measurements

During a 15-day period in late July/early August 2007, we successfully completed a full reoccupation of the Southern Illinois Basin GPS network. As in the past, GPS observations consisted of continuous, 36-hour observing sessions, using dual-frequency Trimble GPS antennas, equipped with Dorne-Margolin choke-ring antennas to reduce multipath noise. During this campaign, we used a combination of five Trimble 4000SSi receivers from Indiana University and three Trimble R7 receivers from the UNAVCO instrument pool. We were therefore able to make measurements at eight network sites simultaneously. We were also able to take advantage of a growing number of continuous GPS sites (operated by the NGS CORS network) and of the continuous GAMA network currently operated in the NMSZ by the CERI group. Of the 56 stations, only one was lost (due to a mine reclamation project) and all others were successfully occupied with full data recovery.

Similarly, we conducted a field campaign in August 2008 to reobserve 30 of the 36 sites in the Shawnee National Forest network in southernmost Illinois. Observing criteria were similar to those described above, except that shorter occupation sessions, of 20 to 24 hours, were used. Finally, we conducted a special campaign in the aftermath of the 2008 Mt. Carmel, Illinois earthquake, in order to search for possible coseismic deformation signals associated with the earthquake main shock. The data from these three campaigns have been submitted to the UNAVCO Data Archive which will provide for quality control, long-term archiving, and future access by other members of the community.

Data processing

For a number of reasons, we have elected to transition from our previous application of Bernese and GIPSY processing software to GAMIT/GLOBK [*Herring et al.,* 2006*a*]. Because of this transition, we have had to 'start from scratch', reanalyzing raw data files from the 1997, 2002, and 2007 field campaigns, recompiling instrument, antenna height, and orbit files, along with comparable data from regional and global network sites. We have been greatly assisted in this transition through the generous support of the MIT GPS group (R. King, S. McCluskey), including a one-week site visit by graduate student Gerald Galgana; we continue to work with them through email and telephone consultation. We are using the following data processing strategy [e.g., *King & Bock*, 2004]:

1. Raw GPS data collected in the field (derived from three campaign observations in 1997, 2002 and 2007) are analyzed in 24-hour daily solutions, together with regional and global permanent sites, to estimate loosely constrained positions of survey sites through double-differenced daily phase observations. For these campaign solutions, all conducted since 1997, we take advantage of the improved determination of satellite orbit parameters from a growing global network of GPS tracking stations. In this case, our regional solutions are determined by combining campaign data with a set of 10-14 IGS and CORS continuous sites located within the stable North American Plate. The GAMIT software uses fixed satellite orbits and Earth orientation parameters, atmospheric zenith delays, and satellite clock corrections (provided by NASA, USNO, and IGS) to determine these daily position estimates.
2. Initial coordinates were based on the ITRF 2005 global reference frame [*Altamimi et al.,* 2007]. To account for site-dependent noise primarily coming from multipath errors, we applied elevation-dependent noise models depending on the phase observations. In the processing, we also accounted for effects emanating from long-wavelength site motions due to earth solid-body and ocean loading tides derived from IERS 2003 [*Herring et al.,* 2006*a*].

3. Daily positions of these quasi-observations from GAMIT were then determined in GLOBK [*Herring et al., 2006b*] with respect to a network of nine relatively stable IGS stations, similar to the technique described in *McCaffrey et al.*[2007]. This is accomplished by using a seven-parameter Helmert transformation (translation, rotation, and scale) to minimize relative motion between sites and reference stations. Velocity estimates were then made from least-square linear fits through Kalman filtering of daily positions and covariance matrices of campaign stations and regional continuous GPS sites from 1997, 2002, and 2007. The GLOBK software was then used to determine and tie these position and velocity estimates with respect to a network of around 120 IGS and CORS stations defining the Stable North American Reference Frame (SNARF).

Velocity Analysis

Preliminary results from the first two epochs' measurements (1997-98) were reported by Hamburger et al. [2002]. They reported statistically significant velocities (with respect to sites located outside the WVSZ) for a number of sites surrounding the Wabash Valley Fault System, suggesting systematic sinistral strain along the NNE-trending fault complex—and providing the impetus for continued monitoring of the Wabash Valley seismic zone.

Our new results, based on three epochs of geodetic data now spanning a ten-year period (Figure 3), show a somewhat less dramatic picture of crustal movements, with most of the sites showing markedly lower velocities. Nearly 90% of the sites now show velocities < 1 mm/yr with respect to the local reference frame (with respect to the 'fixed' station BLO-1 on the northeastern edge of the network). The errors have also been significantly reduced. Out of the 56 sites measured, approximately 90% now show velocities < 1 mm/yr. On the other hand, there are some interesting indications of systematic geodetic motion; many of the network sites show a systematic northwestward motion (averaging 0.7 mm/yr) with respect to the Stable North American Reference Frame (SNARF)

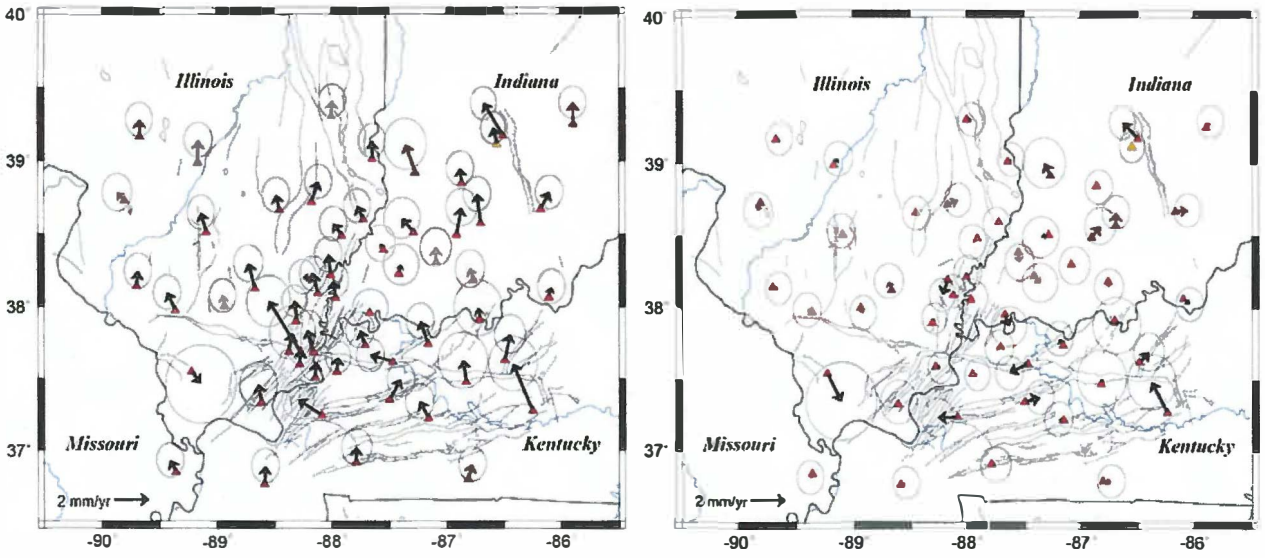

Figure 3: Results of GPS analysis for the Southern Illinois Basin GPS network, 1997-2007. Green lines show mapped faults, as in Figure 2. Figure at left shows velocities with respect to the stable North American reference frame; figure at right shows velocities with respect to 'fixed' station, BLO-1 (yellow triangle).

We also compare our observations with those collected by other networks in the region. Figure 4 shows our network results in comparison with those collected by the Northwestern University campaign network of *Newman et al.* [1999] and the GAMA continuous GPS network of *Smalley et al.* [2006], both reduced to a 'local' reference frame with respect to site BLO1 (in the NE corner of the Illinois Basin network. Note the significantly larger velocities (and error ellipses for the NWU network, which was only observed for a 6-year period from 1991 to 1997. We also note the similar scale of velocities and errors resulting from a ten-year record of measurement at the Illinois Basin network compared with a 3-year record of continuous data from the GAMA network.

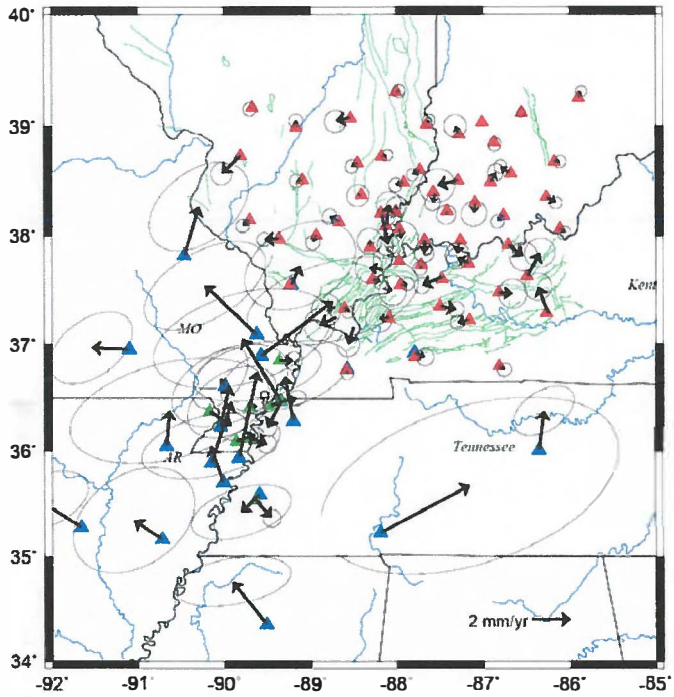

Figure 4. Comparison of velocity estimates from three midcontinent GPS networks: Illinois Basin network (red), NWU New Madrid campaign network (blue), and GAMA continuous GPS network (green). Error ellipses show 1-sigma (65%) confidence interval.

Elastic Block Modeling & Strain Analysis

The newly derived Illinois Basin velocity field can be used to analyze possible crustal motions and internal block strains using two different approaches: an elastic block modeling approach and a continuous strain inversion method. In addition, we combine data from the three networks described above to obtain information about possible regional patterns in strain.

Elastic Block Modeling. We model the study area that considers the behavior of mobile, elastic blocks on a spherical Earth, implemented through the software DEFNODE [*McCaffrey*, 1995]. These tectonic blocks are separated by faults, either locked or freely slipping. Block motions can be constrained by (known) Euler poles and rotation rates, GPS velocities, and slip vectors from earthquake focal mechanisms. Blocks interact by relative rotation along Euler poles, and locking along fault planes, defined by a coupling factor. Block motions can be defined by rigid rotation, or by a combination of rigid rotation, elastic strain due to fault locking, and internal strain. Forward models of block motions (as well as fault coupling) are estimated through inversions relating surface motion with motion at depth using elastic half-space dislocation models [*Okada*, 1985; 1992]. Fault locking is estimated based on integration of coupling along small finite fault

patches, defined by nodes [*McCaffrey*, 2002]. The best-fit model is obtained by comparing observed and predicted motions, with the errors minimized by least squares through the simulated annealing/simplex minimization technique.

We model the lithosphere in the immediate Wabash Valley-New Madrid area using various approaches:

1. A single-block model (treating the entire study area as a single, internally deforming block)
2. A two-block model, comprised by a NW block and a SE block, separated by a NE-SW-trending fault which represents the Wabash Valley Fault System or Commerce Geophysical Lineament);
3. A four-block model, comprised by NE, NW, SE and SW blocks, separated by a NE-SW trending Wabash Fault, and a W-E trending Cottage Grove and Rough Creek Graben Fault System;
4. An eight-block model, which divides the region into eight regions based on their proximities to certain fault zones, essentially emulating a continuous deformation network.

We show here initial results of the four-block model which combine GPS velocities from the IU network (1997, 2002, and 2007 campaign data), GAMA sites [*Smalley et al.*, 2005], and Northwestern University [*Newman et al.*, 1999]. The model successfully matches the general NW-trend of western block/s, and a N to NNW trend in the motion of NE/E blocks; The motion along the plane/line defining the Wabash Fault system is essentially sinistral strike-slip, with similar sinistral shear motions—with a component of transtension or transpression—along the Cottage Grove-Rough Creek Graben Fault system. The modeling suggests fault slip rates essentially indistinguishable from zero (ranging from ~0.2 to 0.5 mm/yr) between defined blocks. Coupling estimates from best-fit models reveal essentially no locking along both faults.

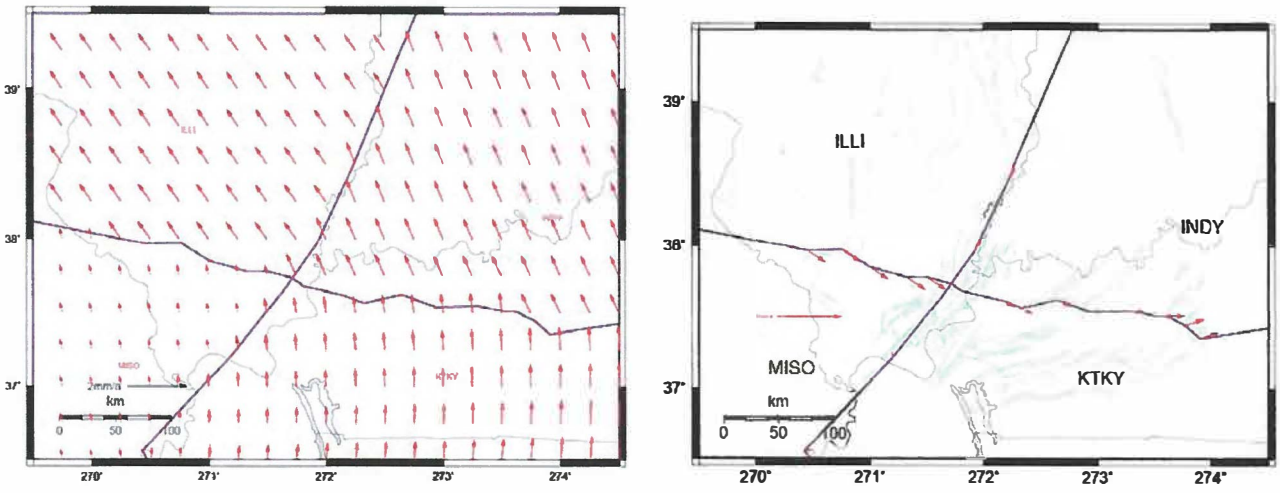

Figure 5: Results of elastic block modeling analysis using data from GPS networks in the U.S midcontinent. Results are shown for four-block model with free rotation with respect to North American plate and fault-locking strain between blocks. Green lines show mapped faults, as in Figure 2. Figure at left shows modeled block velocities with respect to the stable North American reference frame; figure at right shows inferred fault slip rates along block-bounding faults.

Figure 6 shows results for the four-block model and a single, one-block model inverting only for internal block strain (i.e., no motion is allowed to take place between blocks). Both models suggest predominant north-south to NNW-SSE extension, with a variation in the presence and relative magnitude of east-west compression. The strain inversion shown in Figure 6a uses only the Southern Illinois Basin GPS network velocities, and reveals about NNE-SSW extension at a rate of 2.5 nanostrain/yr and WNW-ESE compression at a rate of 0.8 nanostrain/yr.

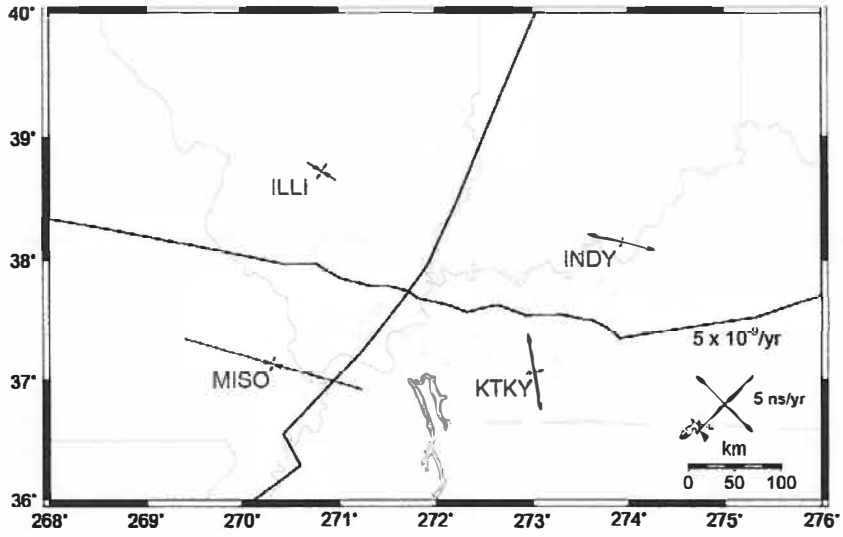

Figure 6: Results of elastic block modeling for four-block model with internal strain only. Green lines show mapped faults, as in Figure 2. Arrows indicate modeled block internal strain; legend indicates scale for 5 nanostrain/yr.

Continuous Deformation Modeling. We also examine a suite of models of crustal strain derived from the Illinois Basin velocity field through direct inversion of the GPS velocity field for principal strain directions. A mesh is generated with GPS sites at vertices of triangles generated with Delaunay triangulation. The three components of the strain-rate tensor are related linearly to the rate of change of baseline lengths. We invert for the strain-rate tensor using damped least squares with a second-derivative (Laplacian) smoothing constraint. The relative weight placed on damping the solution and fitting the data is optimized using a Bayesian inversion scheme. With this inversion scheme we are trying to determine whether or not a long-wavelength, spatially smooth deformation field can be extracted from the noisy data. Figure 7a shows the result with optimal weighting and Figure 7b shows a result with less weight on smoothing. The optimal strain-rate field shows uniform N/S and E/W principal stretching. This result shows that there is no significant spatial variation in the strain-rate field under the assumptions in the inversion.

Models of Seismicity and Deformation in the southern Illinois Basin

While the highly focused seismic activity in the New Madrid seismic zone has often been attributed to slip on specific basement structures in the Mississippi Embayment [e.g., *Zoback et al.*, 1980; *Johnston and Schweig,* 1996], the cause of the diffuse patterns of earthquake activity in the southern Illinois Basin has remained more enigmatic. In this portion of our study, we apply geodynamic models to examine a suite of possible mechanisms for present-day deformation in this northern periphery of the New Madrid seismic zone. We test the hypothesis that the

southern Illinois Basin seismicity and deformation is not an isolated consequence of far-field stresses acting on pre-existing zones of weakness, but rather a consequence of a perturbation of the stress and deformation field due to the New Madrid earthquakes.

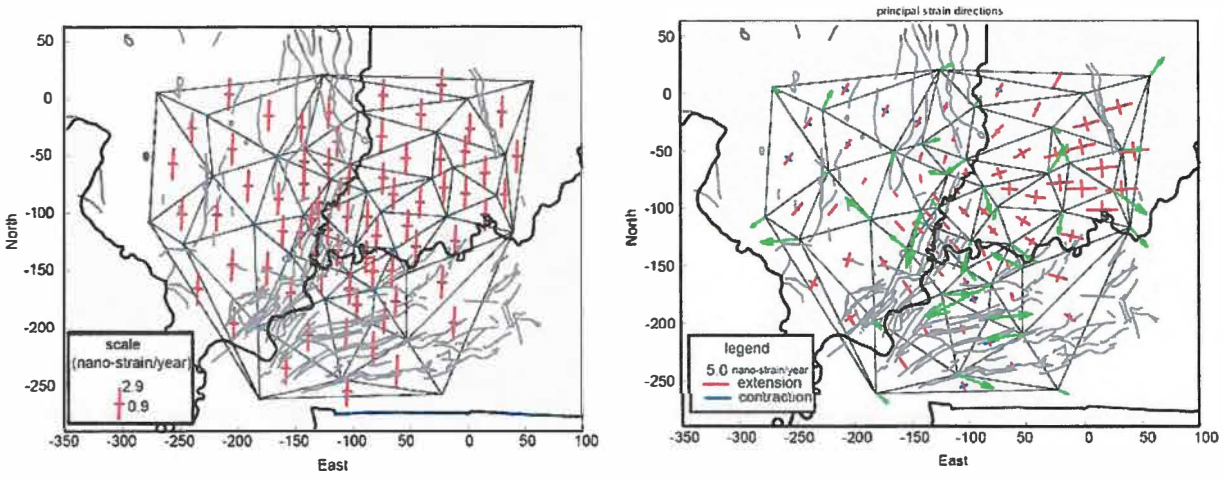

Figure 7. Inverted strain-rate fields using damped least squares inversion. Field on the left is computed with optimal weighting between data fit and smoothness. Field on the right is arbitrarily smoothed to show some spatial variation of strain-rates

Seismic activity in midcontinent regions is often modeled as a manifestation of far-field tectonic stresses acting on zones of weakness within a continental lithosphere [e.g., *Zoback et al.,* 1980; *Liu & Zoback*, 1997; *Newman et al.,* 1999]. There are, however, alternate models for intraplate seismicity, based on the concept that earthquakes could result from time-varying response to local stress perturbations [e.g., *Kenner & Segall,* 2000; *Pollitz et al.,* 2002]. It has been proposed that the anomalous microseismicity that characterizes the present-day New Madrid seismic zone may actually represent an aftershock sequence of the 1811-1812 earthquakes [e.g., *Mueller et al.,* 2004; *Stein & Newman*, 2004], but this idea has not been tested quantitatively. A long aftershock sequence is plausible, particularly in the low-strain-rate midcontinent, given the theoretical inverse relationship between aftershock duration and stressing rate derived by *Dieterich* [1994] from rate- and state-dependent friction.

We examine the extent to which present-day seismicity and strain rates in the New Madrid seismic zone and Illinois Basin can be attributed to stress changes from the 1811-1812 earthquakes. *Dieterich* [1994] derived a relationship between a perturbation in stress to a steady background stressing rate and the perturbation to a background seismicity rate. The evolution of the ratio of seismicity rate after the stress perturbation, R, to the background stressing rate, r, is

$$\frac{R}{r} = \frac{1}{\gamma \dot{S}_r}, \quad d\gamma = \frac{1}{A\sigma}(dt - \gamma dS) \qquad (1)$$

where γ is a state variable that evolves with time, S is shear stress, $\dot{S}_r$, is background stressing rate, σ is effective normal stress, and A is a dimensionless friction parameter, usually in the range 0.005-0.015. This relationship provides a basis for predicting seismicity rates from the stress perturbation following the New Madrid earthquakes.

We model the stress evolution following the New Madrid earthquakes in an elastic lithosphere overlying a viscoelastic asthenosphere. The elastic lithosphere is stressed by imposed sudden slip events that simulate New Madrid earthquakes and corresponding viscoelastic flow in the asthenosphere [e.g., *Pollitz et al.,* 2001]. We use the fault geometry of *Mueller et al.* [2004] as a guide and approximate the 1811-1812 earthquakes with 4 m of slip on a 60 km-long vertical strike-slip fault to represent slip on the NE trending Cottonwood Grove fault and 5 m of slip on a 40 km long, 45° dipping reverse fault to represent slip on the NW trending Reelfoot thrust. In some models we include slip on a strike-slip fault in southern Illinois to represent a possible third New Madrid earthquake outside of the New Madrid Seismic zone, as proposed by *Hough et al.* [2005]. The elastic thickness is assumed to be 25 km. We varied the asthenosphere viscosity over four orders of magnitude (10^{18}-10^{20} Pa s) and adjusted $A\sigma$ "by eye" to get a reasonably good fit between observed and computed seismicity rates. To solve for the evolution of seismicity rate, we calculate the evolution of stress following the earthquake and convert this to seismicity rate using equation (1). The stress change in equation (1), dS, is the shear stress change in the direction of fault slip. However, since it is not possible to know the orientation of faults that produce the seismicity in the Wabash Valley region, we simply regard dS in equation (1) as the change in maximum shear stress because this does not require *a priori* knowledge of the fault orientation.

Figure 8 shows the velocity and strain rate field at 190 years following the New Madrid earthquakes (present day) for asthenosphere viscosity of 10^{19} Pa s. The predicted surface velocities in the vicinity of the Wabash Valley Seismic Zone are generally directed eastward with magnitude of 0.5 mm/yr or less. The strain pattern in southern Illinois and Indiana generally shows E/W principal shortening and N/S principal extension. The present-day strain rates are relatively large in the vicinity of the New Madrid earthquakes.

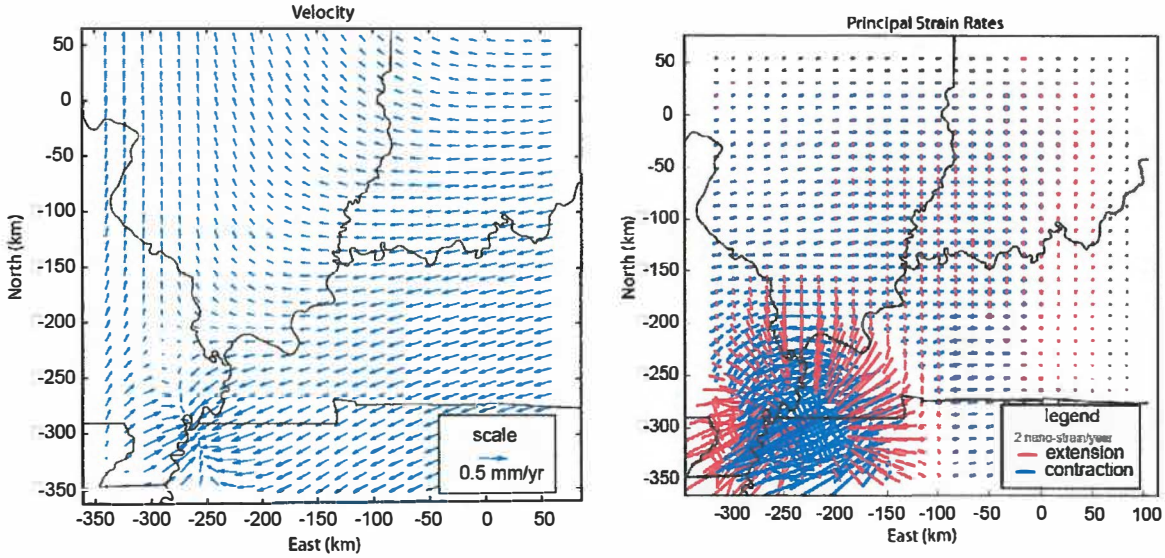

Figure 8. Modeled present-day surface velocities and principal strain-rate directions assuming New Madrid earthquakes in a 25 km thick elastic lithosphere overlying an asthenosphere with viscosity of 10^{19} Pa s.

The computed and modeled seismicity rates are shown in Figure 9 for asthenosphere viscosity of 10^{19} Pa s. To obtain the modeled patterns, it is necessary to set $a\sigma$ = 0.05 MPa, which corresponds to a low value of σ = 5 MPa for laboratory values of a = 0.01, which would could be achieved with high pore fluid pressure. We find a background stressing rate of ~5 Pa/yr, corresponding with a strain rate of about 5×10^{-9}/yr, which seems appropriate for the mid-continent setting. The bottom-right panel in Figure 9 shows the predicted present-day seismicity rate assuming slip only the two major faults in the New Madrid Seismic Zone. The bottom-left panel in Figure 7 shows the predicted present-day seismicity rate assuming the third earthquake outside of the New Madrid Seismic zone in southern Illinois. The seismicity rate pattern in the bottom-left panel is more nearly consistent with observed asymmetric seismicity rate distribution. This modeling shows that the Wabash Valley seismicity may indeed be a prolonged aftershock sequence following the New Madrid earthquakes.

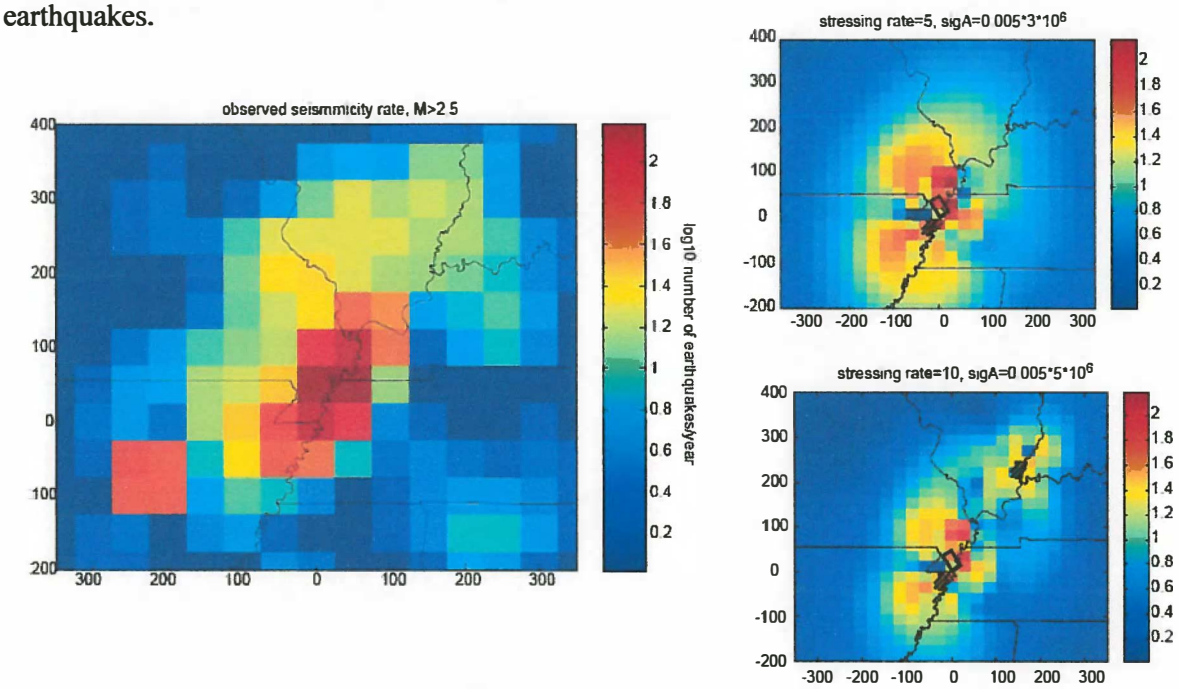

Figure 9. Observed and predicted seismicity rate in the U.S. midcontinent, based on viscoelastic relaxation following the 1811-1812 New Madrid earthquakes, combined with a rate-state friction model of earthquake triggering. Colors correspond to logarithmic relative seismicity rates (with respect to 'background' rates), as labeled. Figure at lower left shows predicted seismicity rate based on a relatively high stressing rate and the presence of a secondary earthquake source in the Wabash Valley seismic zone, as proposed by Hough et al. [2005] ; figure at lower right shows predicted seismicity with a lower stressing rate and without the presence of the Wabash Valley earthquake source.

The April 18, 2008 Mt. Carmel, Illinois earthquake

On 18 April 2008, we were granted an unusual opportunity to observe midcontinent seismicity, when the Wabash Valley of southern Illinois was struck by a moderate-sized (*Mw* 5.2) earthquake, the largest event to have occurred in the central U.S. in the previous 40 years. The earthquake caused moderate damage in the epicentral area and was widely felt throughout the central U.S. [*Herrmann et al.*, 2008]. The intraplate event occurred near the northern

termination of the Wabash Valley Fault System (WVFS). The earthquake was the fifth M>4.5 earthquake to occur in the WVSZ in the past half-century, and was located within 20 km of the recent M 5.0 1987 Olney, Illinois earthquake [*Taylor et al.,* 1988; *Hamburger and Rupp,* 1988]. Its source mechanism, characterized by nearly pure strike-slip faulting under ENE-WSE oriented compressional stresses, was also typical of most earthquakes in this area. The main shock was followed by an unusually rich sequence of aftershocks, with over 250 events recorded in the month following the main shock with magnitudes ranging from 0.7 to 4.5. We used USGS resources to develop an aftershock monitoring campaign, in conjunction with the University of Memphis. We conclude that the earthquake occurred not on the neighboring NNE-trending New Harmony – Mt. Carmel Fault, but on a transverse structure orthogonal to the WVFS.

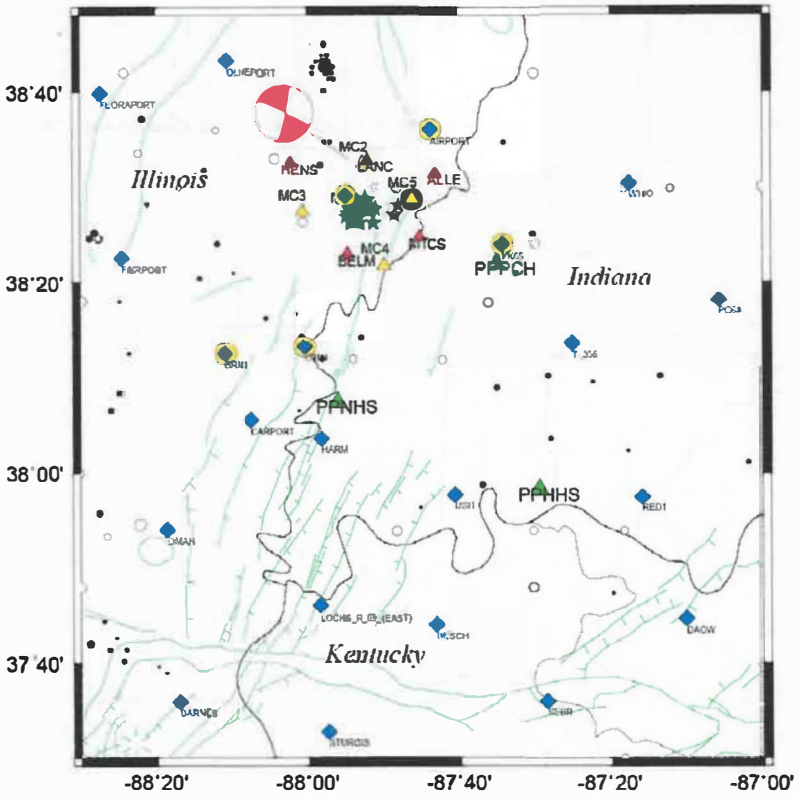

Figure 10. Location of the 2008 Mt. Carmel, Illinois earthquake. Large blue star and small green stars show locations of main shock and aftershocks, respectively. Faults are indicated by green lines. Blue triangles show locations of GPS campaign stations, with circles showing sites that were reoccupied following the earthquake. Red and yellow triangles show temporary stations deployed by IU and CERI, respectively. Green triangles show permanent stations of the Indiana PEPP seismic network. Black dots indicate background seismicity, as recorded by the regional seismic network.

The Mt. Carmel mainshock was followed by a relatively productive aftershock sequence, with at least six felt aftershocks of M>3 [*Herrmann et al.,* 2008]. In an effort to maximize observations of the aftershock sequence, teams from Indiana University (IU) and University of Memphis Center for Earthquake Research and Information (CERI) deployed temporary seismographs in the epicentral area (Figure 10). In total, the group deployed four broadband three-component instruments, six broadband vertical instruments, and two strong-motion accelerographs. The first instruments were deployed at ~23:00 UTC (18:00 CDT), with additional instrument deployment taking place over the next 24-48 hours. The CERI instruments were Guralp CMG6-TD, a 3-component broadband seismometer with an instrument response flat to input ground velocity above 0.033 Hz to the upper limit imposed by the anti-alias filter for sampling at 100 sps. The IU instruments were vertical-component, Guralp PEPP-V broadband seismometers, with a flat

response to velocity above 0.05 Hz to the upper limit imposed by the anti-aliasing filters for the 40 sps data. Instruments were deployed in a roughly circular array, approximately 8 km radius, with CERI and IU stations located within 1 km of the epicenter. All seismometers were located in areas of unconsolidated sediment, and most were located near populated areas. Noise levels were highly variable as a function of location and time of day. However, the proximity to the aftershock source area and the relatively large number of aftershocks yielded over 174 events recorded by three or more stations.

In order to better constrain the spatial pattern of aftershocks, we applied an alternative and novel method of refining relative hypocentral locations based on P wave cross correlation. Our approach involves combined analysis of suites of seismograms within 'event gathers' of hypocenters located in close spatial proximity. We computed arrival times by source-side array processing using a recently developed program called *dbxcor* [Pavlis and Vernon, 2009]. The *dbxcor* program allows user-interactive, waveform correlation of all waveforms linked to one or more control points. The advantage of our approach is that it provides a high degree of confidence in all our waveform correlation arrival-time estimates because all have been reviewed interactively for consistency. Finally, we took the averaged arrival times produced by waveform and relocated the entire aftershock sequence using a program called dbpmel (http://www.antelopeusersgroup.org/). *dbpmel* is an updated implementation of the PMEL [*Pavlis and Booker,* 1982] and SELM [*Pavlis and Hokanson*, 1985] algorithms adapted for three dimensional Earth structure. PMEL and SELM are forms of joint hypocenter determination (JHD) methods that assume that three-dimensional variability in earth structure can be cast into a set of "station corrections". This relocation procedure permitted us to obtain precise relocations of 114 of the initial 171 single-event locations. Initial and final event locations are shown in Figure 11.

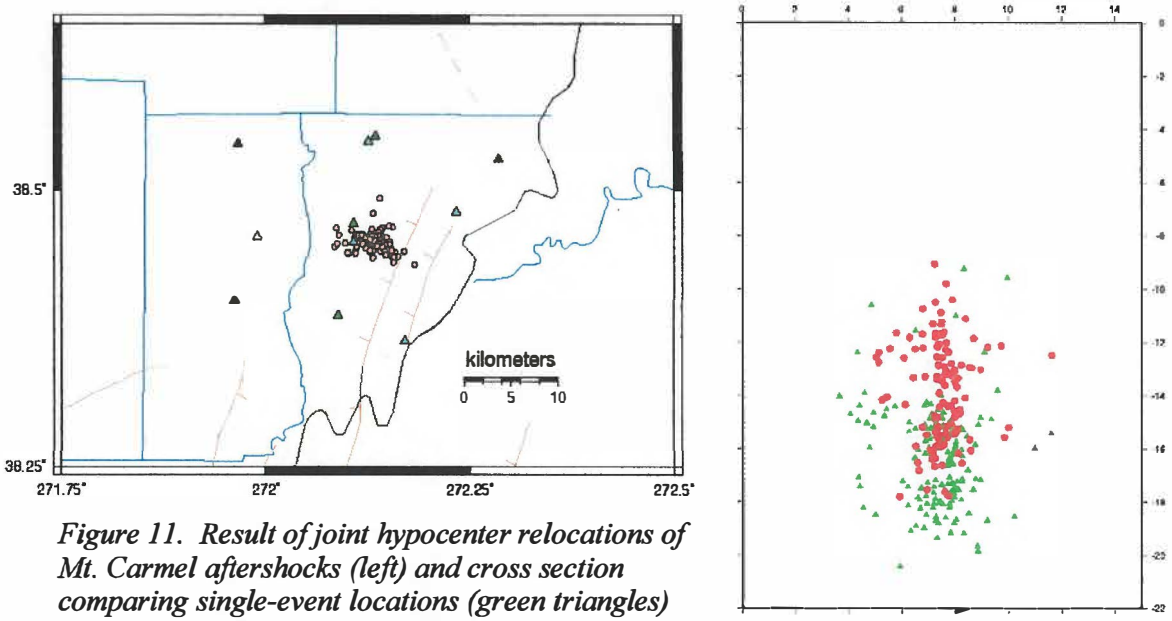

Figure 11. Result of joint hypocenter relocations of Mt. Carmel aftershocks (left) and cross section comparing single-event locations (green triangles) with relocated hypocenters (red circles) (right).

Our results indicate that the relocated aftershock hypocenters are concentrated within a localized area near the northern termination of the New Harmony-Mt. Carmel fault (Figure 11). The vast majority are located within a concentrated cluster of about 6 x 4 km and aligned along a linear trend. The hypocenters align in an ESE-WNW orientation, orthogonal to the surface trace of the New Harmony-Mt. Carmel fault. The hypocentral depths range from 10-18km, with an average depth of 14 km. Our results are consistent with those of *Yang et al.* [2009], who identified an ESE-striking fault plane based on relocation of regional aftershock recordings. Their best-fit solution for the fault plane was striking 292°±11° and dip of 81°±7°. Based on our aftershock relocations we calculate the orientation of the best-fitting fault plane to be striking 290° and dipping 85°. In cross section (Figure 11b), hypocenters define a near-vertical plane, striking 296° and dipping 87°.

The 2008 Mt. Carmel aftershocks provide important constraints on the mainshock location and inferred fault rupture. Because earthquakes in stable continental interiors occur so infrequently, we rely on well recorded aftershock sequences to illuminate seismogenic structures—and thus to help constrain potential for future, larger intraplate events. The recent aftershock sequence shares many characteristics with the 1987 Claremont aftershock sequence. First, both sets of events occurred close to the northern termination of the Wabash Valley Fault System, near its transition to the NNW-trending La Salle belt. Both events were located within the crystalline basement. The 2008 sequence tended to have a slightly greater hypocentral depth of 7-16 km compared with the estimated 7-12 km depth of the 1987 sequence [*Taylor et al.,* 1989; *Langer and Bollinger*, 1991]. Both sets of events produced rich aftershock sequences, in contrast to the 1968 Carbondale, Illinois and the 2002 Caborn, Indiana events, which were nearly devoid of recorded aftershocks.

Initial analysis of the mainshock location and its mechanism [e.g., *Herrmann et al.,* 2008] led to the conclusion that the probable fault plane was coincident with the trend of the New Harmony-Mt. Carmel fault (Figure 10), as well as with the overall NNE-SSW trend of the WVFS. This interpretation follows that of *Kim* [2003], who suggested that the NNE-SSW oriented fault plane of the 2002 Caborn earthquake provided evidence of motion along the Caborn Fault—the first example of a Wabash Valley earthquake that could be correlated with a specific seismogenic fault. Our results, however, lead to a rather different interpretation: that the aftershocks occurred along a near-vertical fault oriented nearly orthogonal to the trend of the New Harmony-Mt. Carmel fault (Figure 11), and not coinciding with any mapped structure in the region.

We examine three possible interpretations of the unusual, cross-strike seismogenic structure illuminated by the 2008 aftershock sequence. First, as proposed by *Yang et al.* [2009], the faulting could be indicative of an accommodation structure intervening between the Wabash Valley Fault System and the LaSalle Anticlinal Belt. Because both of these structures are interpreted to have initiated during the late Precambrian [*Marshak and Paulson,* 1996], this would imply that the accommodation structure was part of a pre-existing structure associated with a transition between these two deformation zones. Such accommodation zones are common to rift structures, where half-graben structures terminate and are tectonically linked to neighboring structures. An alternative interpretation rests on the observation that the unusual aftershock sequence coincides with the termination of the largest of the Wabash Valley faults: The New Harmony – Mt. Carmel Fault. This coincidence might suggest that the fault rupture is the result of a stress concentration associated with the termination of the WVFS. Finally, we note that the aftershock sequence occurs at a high angle (~60°) to an inferred basement structure,

the Commerce Geophysical Lineament [*Hildenbrand & Ravat*, 1997]. Thus, the fault rupture here might be considered to be a secondary Reidel shear associated with a major, through-going primary shear structure.

Magnitude and Time Distribution of Aftershocks

Aftershock magnitudes were determined by calibrating the local aftershock recordings by comparison with amplitudes recorded for the four largest aftershocks for which moment magnitudes were determined by *Herrmann et al.* [2008]. We use these magnitudes in order to analyze the productivity and size distribution of this aftershock sequence, and compare it with other in stable continental interiors, as recently reviewed by *Ebel* [2009]. The overall distribution of aftershocks as a function of time and magnitude is presented in Figure 13. As noted above, the aftershock productivity for moderate-sized events in the WVSZ varies widely; several events produced few or no aftershocks, while others triggered prolific aftershock sequences. This event produced an unusually rich aftershock sequence, which extended at least 30 days after the mainshock, and included at least a dozen felt events, including ten of M>3 and four of M>4 (Figure 12a). The five largest aftershocks occurred at 3 minutes, 5.6 hours, 68 hours, and 175 hours after the mainshock. The largest aftershock (M4.6), which occurred at 1514 UTC on April 19 (5.6 hours after the mainshock) was strongly felt throughout the region. In contrast with most events in stable continental interiors, this magnitude difference (0.6 units) is far smaller than most earthquakes in stable continental interiors, where the mean is 1.4 ± 0.7 magnitude units [*Ebel*, 2009]. The Mt. Carmel sequence contrasts sharply with the most recent moderate-sized earthquake in the region, the Mw 4.6 2002 Caborn earthquake. That event produced no aftershocks recorded by the regional network [*Kim*, 2003], and only one probable aftershock (M2.2) recorded by a local seismic network [*Webb et al.*, 2006], resulting in a magnitude difference of 2.4.

Like most aftershock sequences, there was a strong inverse correlation between magnitude and cumulative number, following the classic Gutenberg-Richter magnitude-frequency relation

$$\log N = A - bM$$

where N is the cumulative number of aftershocks above magnitude M, and A and b are empirical constants (Figure 12b). Analysis of the Mt. Carmel aftershock sequence revealed constants of A= 2.893 and b=.579, respectively. This b-value is anomalously low, both by California standards (0.872 ± .171; *Reasenberg and Jones*, 1989] and in stable continental interiors (0.865 ± .226; *Ebel*, 2009]. This low b-value reflects the unusually large number of high-magnitude aftershocks relative to the mainshock size. However this value compares well with the b-values determined by *Ebel* (0.56] and by *Yang et al.* [2009] (0.6), based on smaller data sets.
We also analyzed the productivity of aftershocks using the modified Omori law relationship, which was recast by Reasenberg and Jones as

$$\lambda(M,t) = 10^{a+b(Mm-M)}(t+c)^{-p}$$

where $\lambda(M,t)$ is the rate of aftershock productivity as a function of magnitude and time, Mm and

M are the magnitudes of mainshock and minimum magnitude range, respectively, and = ***a***, ***b***, ***c***, and ***p*** are empirical constants. We adopt the value ***b*** = 0.579, as determined from the magnitude-frequency relation, and constant ***c*** = 0.05, as defined by *Reasenberg and Jones* [1989] for California data. With these values fixed, the remaining constants ***a*** and ***p*** are determined by least-squares. We obtain the values ***a*** = -0.662 and ***p*** = 1.152 for the Mt. Carmel sequence. The ***p***-value is close to the value of 1.0 determined by *Yang et al.* [2009], but is significantly higher than the 0.78 determined by Ebel [2009]. It is well within the ranges estimated for California (1.060 ± .221; *Reasenberg and Jones*, 1989) and for SCR regions (1.046 ± .221; *Ebel,* 2009). The ***a***-value we obtained (-0.662) departs more significantly from Ebel's estimate (-1.20), and is not directly comparable with Yang et al.'s result as the Omori relation was parameterized differently. Our value falls at near the upper limit of the ranges estimated for California (-1.800 ± .578; *Reasenberg and Jones*, 1989) and for SCR regions (-1.815 ± .821; *Ebel*, 2009). However, this value, which describes absolute aftershock productivity, is highly sensitive to the minimum magnitude used for computing aftershock productivity; thus, it is difficult to compare directly with values obtained by others with different magnitude thresholds. Its relatively large value reflects the unusually high productivity of aftershocks in this sequence.

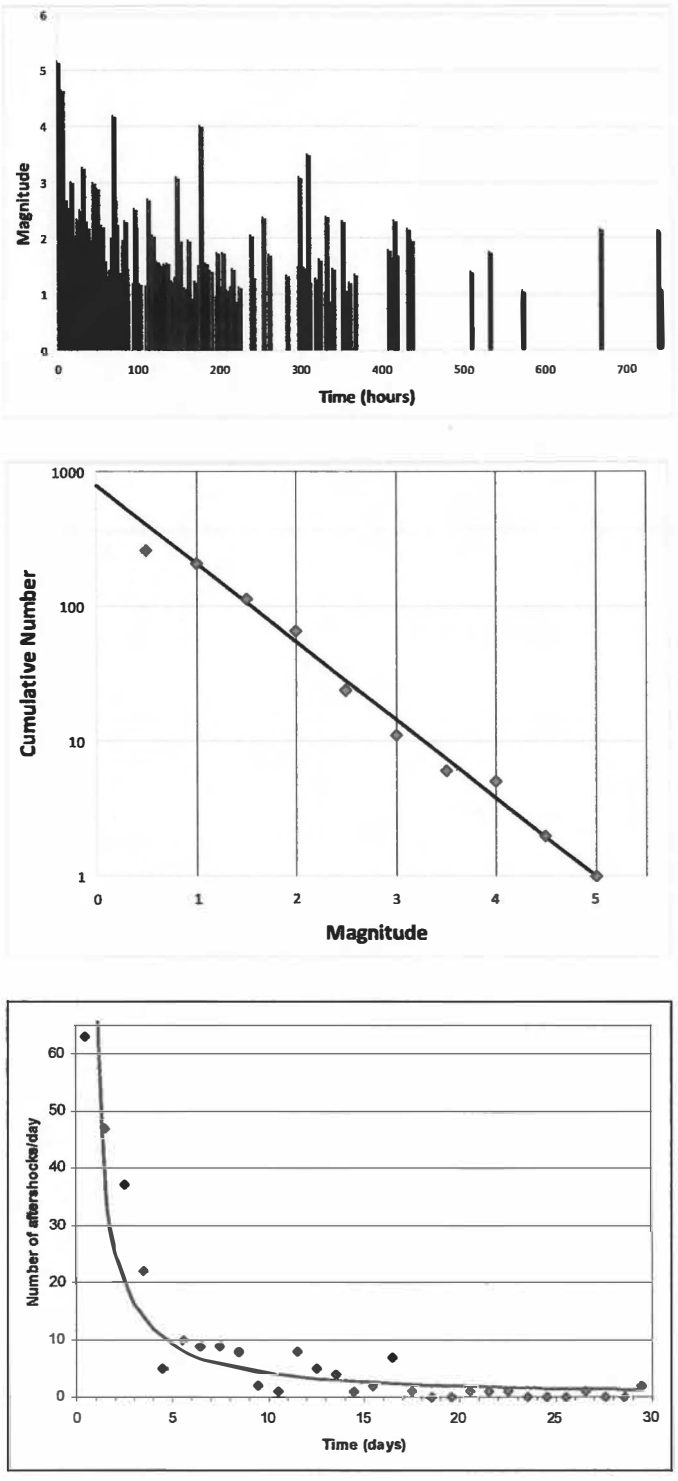

Figure 12. Magnitude and time distribution of aftershocks of the Mt. Carmel earthquake. (A) magnitude distribution as a function of time; (B) magnitude-frequency relation for aftershock sequence; (C) aftershock productivity as a function of time.

Bibliography (Publications Resulting from this Project)

Galgana, G.A., and M.W. Hamburger (2010), Geodetic Observations of Active Intraplate Crustal Deformation in the Wabash Valley Seismic Zone and the Southern Illinois Basin, Seism. Res. Lett., in review.

Hamburger, M.W., K. Shoemaker, G.L. Pavlis, S.P. Horton, M. Withers, and H. Deshon (2010), Aftershocks of the 2008 Mt. Carmel, Illinois Earthquake: Evidence for Conjugate Faulting near the Termination of the Wabash Valley Fault System, *Seism. Res. Lett.*, in prep.

Abstracts

Shoemaker, K, M.W. Hamburger, G.L. Pavlis, S.P. Horton, M. Withers (2009), Hypocentral Relocations of the 2008 Mt. Carmel, Illinois Aftershock Sequence [abstract], *EOS, Trans. Am. Geophys. Un., 90(52), Fall Meet. Suppl.* Abstract S51B-1421

M. Hamburger, Galgana, G., Q. Chen, and K. Johnson, Geodetic Observations From the Region Surrounding the M 5.2 Mt. Carmel, Illinois Earthquake [abstract], *EOS, Trans. Am. Geophys. Un., 89(53), Fall Meet. Suppl.* Abstract G21A-0664.

Horton, S.P., S. Ayele, T. Stigall, G. Pavlis, H. Deshon, M. Hamburger , and M. Withers, Aftershocks of the Mw 5.2 April, 18, 2008, Mt. Carmel, Illinois Earthquake [abstract], *Seismol. Soc. of Amer., Eastern Section, Program & Abstracts*, p. 30.

M.W. Hamburger, G. A. Galgana, K. M. Johnson, R. W. King, Crustal deformation in the Wabash Valley Seismic Zone based on ten years of GPS campaign measurements, *UNAVCO Science Workshop, Program & Abstracts.*

M. Hamburger, Galgana, G., Q. Chen, and K. Johnson, Is There a Connection Between Seismicity and Deformation in the New Madrid and Wabash Valley Seismic zones? [abstract], *EOS, Trans. Am. Geophys. Un., 88(52),* Fall Meet. Suppl. Abstract T51D-0766, 2007.

M. Hamburger, 2008, Active Crustal Deformation in the Southern Illinois Basin [abstract], *EarthScope National Meeting, Monterey, CA, March, 2007, p. 74.*

Student Theses

Galgana, G. (2009), Geodetic Investigations of Active Crustal Deformation in the Philippine Plate Boundary Zone and the Intraplate Region of the Central United States, Ph.D. dissertation, Indiana University, 242 pp.

Shoemaker, K. (2009), Aftershock Relocations of the 2008 Mt. Carmel Earthquake Sequence, B.S. thesis, Indiana University, 52 pp.

REFERENCES

Ault, C. H. and D.M. Sullivan (1982). Faulting in southwest Indiana, *Geological Survey, National Regulatory Commission Pub.* **CR-2908**, 51p.

Ault, C. H., D. Harper, C. R. Smith, and M. A. Wright (1985). Faulting and jointing in and near surface mines of southwestern Indiana, U.S. Nuclear Regulatory Commision, Rept. NUREG/CR-4117, 50 pp.

Bear, G.W., J.A. Rupp and A.J. Rudman (1997). Seismic interpretation of the deep structure of the Wabash Valley Fault System, *Seism. Res. Let.* **68**, 624-640.

Bear, G.W (1997). Integration of seismic reflection and potential field analyses: architecture of Precambrian sedimentary basins in Indiana, Illinois, and Kentucky, Ph.D. dissertation, Indiana University, 171pp.

Bennett, R.A., R.E. Reilinger, W. Rodi, Y. Li, and M.N. Toksöz (1995). Coseismic fault slip associated with the 1992 Joshua Tree, California earthquake: Implications for the Joshua Tree-Landers earthquake sequence, *J. Geophys. Res.*, **100**, 6443-6461.

Blakely, R.F. and M.M. Varna (1976). The seismicity of Indiana described by return periods of earthquake intensities, *Indiana Geological Survey Occassional Paper* **16**, 13 pp.

Bock, Y., R. M. Nikolaidis, P. J. de Jonge, M. Bevis, Instantaneous geodetic positioning at medium distances with the Global Positioning System, *J. Geophys. Res., 105(B12),* 28223-28254, 10.1029/2000JB900268, 2000.

Boucher, C. Z. Altamini, M. Feissel, and P. Sillard (1996). Results and analysis of the ITRF94, *IERS Tech. Note 20,* 191 pp. Int. Earth Rotation Serv., Paris,.

Braile, L. W., W. J. Hinze, J. L. Sexton, R. G. Keller, and E. G. Lidiak (1982). The northeastern extension of the New Madrid seismic zone. *U.S. Geol. Surv. Prof. Paper* **1236**, 175-184.

Braile, L. W., W.J. Hinze, J.L. Sexton, G.R. Keller, and E.G. Lidiak (1986). Tectonic development of the New Madrid Rift Complex, Mississippi embayment, North America, *Tectonophysics*, **131**, 1-21.

Calais, E., G. Mattioli, C. DeMets, J.-M. Nocquet, S. Stein, A. Newman, and P. Rydelek (2005). Seismology: Tectonic strain in plate interiors? *Nature,* **438**, E9-E10 doi:10.1038/nature04428.

Calais, E., J.Y. Han, C. DeMets, J.M. Nocquet (2006). Deformation of the North American Plate Interior from a Decade of Continuous GPS Measurements, *J. Geophys. Res.,* in review.

Chen, Q., M. Hamburger, and J. Rupp (2006). Intraplate strain in the southern Illinois Basin, *Seism. Res. Lett.,* in prep.

Dieterich, J. (1994). A constitutive law for rate of earthquake production and its application to earthquake clustering, *J. Geophys. Res.*, **99**, 2601-2618.

Eagar, K. C., G. L. Pavlis, and M. W. Hamburger (2006). Evidence of possible induced seismicity in the Wabash Valley Seismic Zone from improved microearthquake locations, *Bull. Seism. Soc. Amer.,* in review.

Freymueller, J. T., M. H. Murray, P. Segall, and D. Castillo (1999). Kinematics of the Pacific-North America plate boundary zone, northern California, *J. Geophys. Res.*, **104**:7419-7441.

Freymueller, J. T., S. C. Cohen, and H. J, Fletcher (2000). Spatial variations in present-day deformation, Kenai Peninsula, Alaska, and their implications, *J. Geophys. Res.*, **105,** 8079-8107.

Fraser, G.S., T.A. Thompson, G.A. Olyphant, L. Furer, and S.W. Bennett (1997). Geomorphic response to tectonically-induced ground deformation in the Wabash Valley, *Seism. Res. Let.* **68**, 662-674.

Freymueller, J., N.E. King, and P. Segall (1994). The co-seismic slip distribution of the Landers earthquake, *Bull. Seism. Soc. Am.*, **84**, 646-659.

Hamburger, M.W. and G.L. Pavlis (2003). New Midwestern seismic network combines research and education, *CUSEC Journal, 9:1*, 17-19.

Hamburger, M. W. and J. Rupp (1988). The June 1987 southeastern Illinois earthquake: Possible tectonism associated with the La Salle Anticlinal Belt, *Seism. Res. Lett.*, **59**, 151-158.

Hamburger, M W, G.L. Pavlis, W.Y. Kim, J.S. Haase, and M. Withers, Seismotectonic Setting of the June 18, 2002, Evansville, Indiana Earthquake: Or What's a Nice Earthquake Like You Doing in a Place Like This? [abstract], *EOS, Trans. AGU, 83(47), Fall Meet. Suppl.,* Abstract S22D-03, 2002.

Hamburger, M.W., V.P. Rybakov, A.R. Lowry, B. Shen-Tu, and J.A. Rupp, 2001, Preliminary Results from a GPS Geodetic Network in the Southern Illinois Basin, *Seis. Res. Lett., 73,* 762-775.

Herrmann, R.B., M. Withers, and H. Benz, 2008, The April 18, 2008 Illinois earthquake; an ANSS monitoring success, *Seism. Res. Lett., 79(6):* 830-843

Hildenbrand, T.G. and D. Ravat (1997). Geophysical setting of the Wabash Valley Fault System, *Seism. Res. Let.* **68**, 567-585.

Hildenbrand, T.G, J.H. McBride, D. Ravat (2002). The Commerce geophysical lineament and its possible relation to Mesoproterozoic igneous complexes and large earthquakes in the central Illinois Basin *Seism. Res. Lett.*, **73**, 640-659.

Hough, S. E., Bilham, R., Mueller, K., Stephenson, W., Williams, R., and J. Odum (2005). Wagon loads of sand blows in White County, Illinois, *Seismological Research Letters,* **76**, 373-386.

Johnston, A.C. and E.S. Schweig (1996). The enigma of the New Madrid earthquakes of 1811-1812, Ann. Rev. Earth Planet. Sci., **24**, 339-384.

Kenner, S.J., and P. Segall (2000). A mechanical model for intraplate earthquakes; application to the New Madrid seismic zone, *Science,* **289**, 2329-2332.

Kim, W.-Y. (2003). The 18 June 2002 Caborn, Indiana, Earthquake: Reactivation of ancient rift in the Wabash Valley seismic zone? *Bull. Seis. Soc. Amer., **93***, 2201-2211.

Kolata, D. R. and W. J. Nelson (1991). Tectonic history of the Illinois basin in *Interior Cratonic Basins*, in Leighton, M. W., Kolata, D. R., Oltz, D. F., Eidel, J. J., (eds.), *American Association of Petroleum Geologists, Mem.* **51**, 263-285.

Larson K. M., J. T. Freymueller, and S. Philipsen (1997). Global plate velocities from the Global Positioning System, *J. Geophys. Res.*, **102,** 9961-9981.

Liu, L., M. D. Zoback, P. Segall (1992). Rapid intraplate strain accumulation in the New Madrid seismic zone, *Science*, **257**, 1666.

Liu, L. and M.D. Zoback (1997). Lithospheric strength and intraplate seismicity in the New Madrid seismic zone, *Tectonics,* **16**, 585-595.

Lu, Y., Liu, L., M. D. Zoback, P. Segall (1993). Strain accumulation in the New Madrid seismic zone: second GPS campaign along the Caruthersville-Marked Tree seismicicty trend [abstr.], *EOS, Trans. Am. Geophys. Un.*, **75**, 1451.

Mann, D., and J. T. Freymueller, Volcanic and tectonic deformation on Unimak Island in the Aleutian arc, Alaska, *J. Geophys. Res.*, **108**, doi:10.1029/2002JB001925.

Mazzotti, S., and J. Adams (2005). Rates and uncertainties on seismic moment and deformation in eastern Canada, *J. Geophys. Res.*, **110,** doi:10.1029/2004JB003510.

McBride, J.H, M.L. Sargent and C.J. Potter (1997). Investigating possible earthquake related structure beneath the southern illinois basin from seismic reflection, *Seism. Res. Let.* **68**, 641-649.

McBride, J.H. and D.R. Kolata (1999). Upper crust beneath the central Illinois basin, United States, *Geol. Soc. Am. Bull.*, **111**, 375-394.

McBride, J.H., T.G. Hildenbrand, W.J. Stephenson, C.J. Potter (2002a). Interpreting the earthquake source of the Wabash Valley seismic zone (Illinois, Indiana, and Kentucky) from seismic-reflection, gravity and magnetic-intensity data. *Seis. Res. Lett., 73,* 660-686.

McBride, J.H, W.J. Nelson, W.J. Stephenson (2002b). Integrated geological and geophysical study of Neogene and Quaternary-age deformation in the northern Mississippi Embayment, *Seism. Res. Lett.*, **73**, 597-627.

Mueller, K., Hough, S. E., and R. Bilham (2004). Analysing the 1811-1812 New Madrid earthquakes with recent instrumentally recorded aftershocks, *Nature,* **429**, 284-288.

Munson, P. J., C. A. Munson, and E. C. Pond (1995). Paleoliquefaction evidence for a strong Holocene earthquake in south-central Indiana, *Geology*, **23**, 325-328 .

Munson, P. J., S. F. Obermeier, C. A. Munson, and E.R. Hajic (1997). Liquefaction evidence for Holocene and latest Pleistocene seismicity in the southern halves of Indiana and Illinois: A preliminary overview, *Seism. Res. Let.* **68**, 521-536.

Nelson, W.J., and D.K. Lumm (1984). Structural geology of southeastern Illinois and vicinity, *U.S. Nuc. Reg. Comm. Rept. NUREG/CR-4036*, 127 pp.

Nelson, W. J. (1991). Structural styles of the Illinois basin in *Interior Cratonic Basins*, in Leighton, M. and others (eds.), *American Association of Petroleum Geologists, Mem.* **51**, 209-243.

Newman, A., S. Stein, J. Weber, J. Engeln, A. Mao, and T. Dixon (1999) Slow Deformation and Lower Seismic Hazard at the New Madrid Seismic Zone, Science, **284**, 622.

Newman, A., J. Schneider, S. Stein, and A. Menez, Uncertainties in seismic hazard maps for the New Madrid seismic zone and implications for seismic hazard communication, Seismological Research Letters, 72; 6, 647-663, 2001.

Newman, A., Stein, S., Weber, J., Engeln, J., Mao, A., and T. Dixon, 1999. Slow deformation and lower seismic hazard at the New Madrid Seismic Zone, Science, 284, no.5414, pp.619-621

Nocquet, J.M., and E. Calais, The crustal velocity field in Western Europe from permanent GPS array solutions, 1996-2001, Geophys. J. Int., 72-88, 2003.

Nuttli, O. W. (1979). Seismicity of the central United States, *Geo. Soc. Am., Rev. Eng. Geol.*, **IV**, 67-93.

Obermeier, S. F., P. J. Munson, C. A. Munson, J. R. Martin, A. D. Frankel, T. L. Youd, and E. C. Pond (1992). Liquifaction evidence for strong Holocene earthquake(s) in the Wabash Valley of Indiana-Illinois, *Seism. Res. Lett.*, **63**, 321-336.

Obermeier, S. F., N. K. Bleuer, C. A. Munson, P. J. Munson, W. S. Martin, K. M. McWilliams, D.A. Tabaczynski, J. K. Odum, M. Rubin, and D. L. Eggert (1991). Evidence of strong earthquake shaking in the lower Wabash Valley from prehistoric liquefaction features, *Science* **251**, 1061-1063.

Obermeier, S.F., R.C. Garniewicz, and P.J. Munson, 1996, Seismically induced paleoliquefaction features in southern half of Illinois [abstract], *Seismol. Res. Lett., 67*, 49.

Palmer, J.R., M. Shoemaker, D. Hoffman, N.L. Anderson, J.D. Vaughn, and R.W. Harrison (1997). Seismic evidence of Quaternary faulting in the Benton Hills area, southeast Missouri, *Seism. Res. Let.* **68**, 650-661.

Park, K.-D., R.S. Nerem, J.L. Davis, M.S. Schenewerk, G.A. Milne, J.X. Mitrovica (2002). Investigation of glacial isostatic adjustment in the Northeast U.S. using GPS measurements, *Geophys. Res. Lett.*, **29**, 4 pp.

Parsons, T., S. Toda, R. S. Stein, A. Barka and J. H. Dieterich (2000). Heightened odds of large earthquakes near Istanbul: An interaction-based probability calculation, *Science,* **288**, 661-665.

Pavlis, G.L. and J. R. Booker (1983), Progressive multiple event location (PMEL), *Bull. Seism. Soc. Am., 73(6, Part A)*:1753-1777.

Pavlis, G., and N. Hokanson (1985), Separated Earthquake Location, *J. Geophys. Res., 90(B14),* 12777-12789.

Pavlis, G.L., A.J. Rudman, B.R. Pope, M.W. Hamburger, G.W. Bear, and H.J. Al-Shukri, 2001, Seismicity of the Wabash Valley Seismic Zone based on a temporary seismic array experiment, *Seis. Res. Lett., 73,* 751-761.

Pollitz, F.F., Kellogg L., and R. Bürgmann (2002). Sinking mafic body in a reactivated lower crust: A mechanism for stress concentration at the New Madrid Seismic Zone, *Bull. Seismol. Soc. Am.,* **91**, 1882-1897.

Pollitz, F. F., Wicks, C., and W. Thatcher (2001). Mantle Flow Beneath a Continental Strike-Slip Fault: Postseismic Deformation After the 1999 Hector Mine Earthquake, *Science,* **293**, 1814-1818.

Ruina, A. (1983). Slip instability and state variable friction laws, *J. Geophys. Res.,* **88**, 10359-10370.

Rupp, J. A., G. W. Bear, M.W. Hamburger, A.J. Rudman, V.P. Rybakov, and A.R. Lowry, (1999). Geophysical and geodetic evidence for upper crustal deformation associated with the Wabash Valley seismic Zone, *Geol. Soc. Am., N. Central Section, Abst. w/ Prog.*, p. 68.

Schilt, F.S., and R.E. Reilinger (1981), Evidence for contemporary vertical fault displacement from precise levelling data from the New Madrid seismic zone, western Kentucky, *Bull. Seismo. Soc. Am.* **71**, 1933-1942.

Schweig, E.S. and J.S. Gomberg (1999). Comment: Caution urged in revising earthquake hazard estimates in New Madrid seismic zone, *EOS, Trans. Am. Geophys. Un.,*

Sexton, J. L., L. W. Braile, W. J. Hinze, and M. J. Campbell (1986). Seismic reflection profiling studies of a buried Precambrian rift beneath the Wabash Valley fault zone, *Geophysics*, **51**, 640-660.

Sexton, J.L., H. Henson, N. Koffi, M. Coulibaly, and J. Nelson (1996). Seismic reflection and georadar investigation of the Barnes Creek area in southeastern Illinois [abstr.], *Seismol. Soc. Am. Ann. Mtg., Suppl. Abs.*

Smalley, R., Jr, M.A. Ellis, J. Paul, R.B. Van Arsdale (2005). Space geodetic evidence for rapid strain rates in the New Madrid seismic zone of central USA, *Nature*, **435**, 1088-1090.

Snay, R. A., J. F. Ni, and H. C. Neugebauer (1994). Geodetically derived strain across the northern New Madrid Seismic Zone, *U.S. Geol. Surv. Prof. Pap.* **1538-F**.

Stauder, W., and O. W. Nuttli (1970). Seismic studies: South central Illinois earthquake of November 9, 1968, *Bull. Seismo. Soc. Am.* **60**, 973-981.

Stein, R.S. (2003). Earthquake Conversations, *Sci. Am.*, **288:1**, 72-79.

Stein, S., and A. Newman (2004). Characteristic and uncharacteristic earthquakes as possible artifacts; applications to the New Madrid and Wabash seismic zones, *Seismological Research Letters,* **75**,173-187.

Taylor, K. B., R. B. Herrmann, M. W. Hamburger, G. L. Pavlis, A. Johnston, C. Langer, and C. Lam (1989). The southeastern Illinois earthquake of 10 June 1987, *Seismo. Res. Lett.* **60**, 101-110.

Wang, Q., P-Z. Zhang, J. T. Freymueller and others (2001). Present-day crustal deformation in China constrained by Global Positioning System measurements. *Science,* **294**: 574-577.

Weber, J., S. Stein, and J. Engeln (1997). Estimation of strain accumulation in the New Madrid seismic zone from GPS geodesy, *Tectonics, 17,* 250-266, 1998.

Wheeler, R. (1997). Boundaries separating the seismically active Reelfoot rift from the sparsely seismic Rough Creek graben, Kentucky and Illinois, *Seism. Res. Let.* **68**, 586-598.

Zoback, M. L., M. D. Zoback, and and 27 others (1989). Global pattern of tectonic stress. *Nature,* **341**, 291-298.

Zumberge, J. F., M. B. Heflin, D. C. Jefferson, M. M. Watkins, and F. H. Webb (1997). Precise point positioning for the efficient and robust analysis of GPS data from large networks, *J. Geophys. Res., 102*, 5005--5018.

Zoback, M.D., R.M. Hamilton, A.J. Crone, D.P. Russ, F.A. McKeown, S.R. Brockman (1980). Recurrent intraplate tectonism in the New Madrid seismic zone, *Science,* **209**, 971-976.

Table 1. Observed velocities of GPS Stations used in this study

WABASH Campaign Sites (48)

Longitude	*Latitude*	*Ve*	*Vn*	*σe*	*σn*	*Correlation*	*Station*	*Group*
273.232	38.192	0.04	-0.32	0.34	0.42	0.018	ADY1	WAB
272.275	38.603	-0.12	-0.14	0.31	0.39	0.015	AIRP	WAB
271.721	37.599	0.28	-0.05	0.29	0.37	0.01	BARN	WAB
271.391	37.336	0.04	0.11	0.43	0.51	0.014	BAY1	WAB
273.443	39.119	0.00	0.00	0.29	0.37	0.011	BLO1	WAB
271.828	38.201	-0.30	-0.88	0.31	0.39	0.009	BRN1	WAB
271.877	38.095	-0.02	0.21	0.31	0.39	0.014	CARP	WAB
271.998	39.304	0.29	-0.01	0.31	0.39	0.007	CASP	WAB
270.908	38.511	-0.08	0.22	0.32	0.40	0.011	CENP	WAB
274.103	39.253	0.21	0.32	0.31	0.38	0.012	COLU	WAB
273.131	38.851	0.14	-0.07	0.32	0.40	0.019	CRA1	WAB
272.211	36.915	0.25	-0.05	0.35	0.42	0.019	EDVL	WAB
271.065	38.005	0.14	-0.29	0.31	0.39	0.013	FAAI	WAB
271.547	38.665	0.04	-0.04	0.32	0.40	0.013	FLOR	WAB
272.089	38.486	-0.26	-0.20	0.32	0.40	0.014	GARD	WAB
273.289	37.919	0.13	-0.29	0.56	0.65	-0.01	GOSP	WAB
272.034	38.062	0.09	0.09	0.35	0.43	0.012	HARM	WAB
273.171	37.477	0.03	0.34	0.57	0.66	-0.004	HART	WAB
272.727	38.921	-0.34	0.71	0.49	0.59	-0.004	HAWT	WAB
270.196	38.731	-0.19	-0.46	0.34	0.43	0.011	JACO	WAB
272.503	37.353	0.86	0.25	0.32	0.40	0.011	KY02	WAB
273.890	38.067	0.37	-0.30	0.32	0.40	0.016	LAC1	WAB
270.330	39.167	0.20	0.04	0.31	0.39	0.009	LITP	WAB
273.185	36.798	0.47	-0.05	0.32	0.39	0.017	LOGA	WAB
271.333	38.130	-0.14	0.49	0.34	0.41	0.014	LOVI	WAB
271.415	36.765	0.27	0.10	0.32	0.39	0.016	MAYP	WAB
270.775	37.550	0.78	-1.62	0.82	0.91	0.019	MKND	WAB
272.842	37.226	-0.29	0.05	0.33	0.40	0.017	MUHL	WAB
273.749	37.280	-0.89	1.73	0.56	0.64	0.005	NOL1	WAB
271.826	38.722	0.61	0.25	0.31	0.39	0.009	OLNE	WAB
271.694	37.902	0.11	0.24	0.29	0.36	0.011	OMAH	WAB
271.992	38.222	0.09	0.22	0.32	0.40	0.013	OTB1	WAB
272.908	38.306	0.20	-0.06	0.36	0.44	0.023	PC64	WAB
270.639	37.977	-0.25	0.09	0.32	0.40	0.009	PINC	WAB
272.450	38.389	0.05	-0.55	0.34	0.42	0.013	PK65	WAB
272.354	39.016	0.22	0.12	0.31	0.39	0.01	ROBP	WAB
273.298	38.576	0.02	0.76	0.32	0.40	0.019	ROL1	WAB
273.822	38.676	0.71	0.04	0.32	0.39	0.016	RUSH	WAB
273.507	37.629	0.52	0.60	0.36	0.44	0.016	SAND	WAB
272.529	37.617	-1.05	-0.52	0.32	0.40	0.013	SEBR	WAB
270.300	38.147	0.31	-0.08	0.32	0.39	0.01	SPAR	WAB
272.044	37.546	0.30	-0.05	0.29	0.37	0.009	STUR	WAB
272.586	38.229	0.33	-0.42	0.41	0.46	0.004	T356	WAB
272.328	37.961	0.25	-0.71	0.41	0.46	0.029	USI1	WAB
270.834	38.990	0.26	0.37	0.33	0.40	0.013	VANP	WAB
273.087	38.494	0.50	0.66	0.36	0.44	0.021	W231	WAB
272.712	38.510	-0.44	-0.11	0.42	0.48	0.044	WHIO	WAB
271.913	37.246	-1.13	-0.02	0.37	0.45	0.013	Z405	WAB

SHAWNEE Campaign Sites (19)

Longitude	Latitude	Ve	Vn	σe	σn	Correlation	Station	Group
272.288	37.737	-0.06	-0.06	0.33	0.41	0.016	BESC	SHW
271.510	37.509	0.23	-0.41	0.52	0.63	0.014	CONC	SHW
271.303	37.193	0.33	-0.43	0.37	0.45	0.028	COPL	SHW
271.396	37.512	-1.41	0.20	0.88	0.98	-0.065	GPS4	SHW
271.290	37.424	1.88	0.04	0.64	0.73	0.046	GPS6	SHW
271.397	37.423	1.81	-0.16	0.49	0.59	0.004	GPS7	SHW
271.292	37.250	0.67	1.28	0.44	0.62	0.009	GURL	SHW
271.728	37.687	-1.57	1.98	0.50	0.60	0.026	HOPS	SHW
271.626	37.688	0.44	0.18	0.53	0.62	0.025	HORS	SHW
271.402	37.673	-0.16	1.11	0.40	0.48	0.029	LEDF	SHW
271.398	37.248	1.34	-0.31	0.51	0.61	0.015	MIDW	SHW
271.525	37.688	0.68	-0.48	0.50	0.60	0.029	PANK	SHW
271.619	37.519	1.32	-0.86	0.59	0.69	0.03	PARI	SHW
271.838	37.687	-0.10	0.35	0.37	0.45	0.015	PEAB	SHW
271.854	37.509	0.29	-0.05	0.37	0.45	0.015	POTT	SHW
271.621	37.427	-0.19	1.06	0.66	0.75	0.063	ROSI	SHW
271.287	37.342	0.31	0.68	0.44	0.53	0.014	STAF	SHW
271.500	37.247	0.84	0.23	0.40	0.48	0.035	STAZ	SHW
271.460	37.812	2.04	0.02	0.53	0.62	0.023	T145	SHW

IGS North American sites (11)

Longitude	Latitude	Ve	Vn	σe	σn	Correlation	Station	Group
281.929	45.956	0.17	-1.85	0.22	0.28	-0.014	ALGO	IGS
295.304	32.370	-0.45	-1.36	0.36	0.41	0.078	BRMU	IGS
272.836	37.746	-0.22	0.38	0.32	0.40	0.014	DAOW	IGS
240.375	49.323	0.95	-0.61	0.20	0.25	-0.022	DRAO	IGS
264.134	50.259	-0.23	-1.74	0.26	0.33	0.002	DUBO	IGS
283.173	39.022	0.39	-0.85	0.23	0.28	0.027	GODE	IGS
255.985	30.681	0.47	-0.71	0.19	0.23	-0.019	MDO1	IGS
268.425	41.772	0.22	-0.66	0.22	0.28	0	NLIB	IGS
251.881	34.302	0.05	-1.12	0.21	0.26	-0.004	PIE1	IGS
307.322	47.595	0.14	-0.69	0.11	0.12	-0.015	STJO	IGS
237.832	52.237	-0.68	-0.98	0.18	0.22	-0.037	WILL	IGS

GAMA/CERI at NMSZ Stations (9)

Longitude	Latitude	Ve	Vn	σe	σn	Correlation	Station	Group
270.356	35.541	0.47	-0.76	0.31	0.40	0.007	CVMS	GAM
270.643	36.847	-0.12	-0.24	0.31	0.40	0.008	MAIR	GAM
270.298	36.120	-0.17	-0.45	0.31	0.40	0.007	MCTY	GAM
270.542	36.417	-0.44	-0.33	0.35	0.45	0.008	NWCC	GAM
269.825	36.370	0.19	-1.88	0.45	0.40	0.006	PIGT	GAM
245.707	50.871	0.65	-2.61	0.28	0.36	0.011	PRDS	GAM
270.300	36.413	-0.40	-0.26	0.31	0.40	0.007	PTGV	GAM
270.655	36.474	0.09	-1.21	0.33	0.42	0.004	RLAP	GAM
270.142	36.089	0.12	-0.06	0.31	0.40	0.01	STLE	GAM

CORS/NOAA Stations (4)

Longitude	Latitude	Ve	Vn	σe	σn	Correlation	Station	Group
275.586	41.277	-0.63	-1.43	0.35	0.45	0.006	DEFI	COR
273.494	39.174	-0.88	0.94	0.30	0.39	0.006	IUCO	COR
275.717	39.431	1.17	-0.73	0.36	0.46	0.008	LEBA	COR
276.850	41.075	-0.44	-1.29	0.35	0.45	0.004	TIFF	COR

Supplementary Table 2.
Principal strain rates from inversions of internally deforming blocks

Single Block

Block	*E1*	σ(*E1*)	*E2*	σ(E*2*)	*Az E1*	σ(*Az E1*)	*Az E2*	σ(*Az E2*)
WABZ	-1.40	0.68	1.58	0.55	-55.23	10.71	34.77	10.71

Multiple blocks

Block	*E1*	σ(*E1*)	*E2*	σ(E*2*)	*Az E1*	σ(*Az E1*)	*Az E2*	σ(*Az E2*)
WWAB	-2.61	3.43	3.67	5.32	-50.60	13.46	39.40	13.46
NCWA	-2.36	2.68	3.42	2.33	-67.85	24.18	22.15	24.18
SCWA	-3.14	2.36	2.04	2.28	-83.31	15.68	6.69	15.68
NEWA	0.73	2.61	4.26	3.11	-124.89	8.34	-34.89	8.34
SEWA	1.24	2.96	2.46	3.73	-7.61	24.59	82.39	24.59
CNMZ	-4.66	7.67	11.23	5.91	24.09	18.41	114.09	18.41

2-block system

Block	*E1*	σ(*E1*)	*E2*	σ(E*2*)	*Az E1*	σ(*Az E1*)	*Az E2*	σ(*Az E2*)
WWAB	-3.03	0.72	0.99	0.60	-77.88	6.29	12.12	6.29
EWAB	1.13	0.85	4.71	0.96	31.52	10.31	121.52	10.31

4-block system

Block	*E1*	σ(*E1*)	*E2*	σ(E*2*)	*Az E1*	σ(*Az E1*)	*Az E2*	σ(*Az E2*)
ILLI	-2.07	1.16	1.34	1.18	-57.42	21.46	32.58	21.46
INDY	0.69	1.42	4.50	1.42	13.67	29.16	103.67	29.16
KTKY	1.27	1.95	4.97	1.86	-99.22	22.65	-9.22	22.65
MISO	-11.59	6.77	1.12	7.94	-73.69	18.24	16.31	18.24

Note:
Sign Convention and Units used
Compression (-); Extension (+)
Principle compressional axis (E1) and principal extensional Axis (E2) units are in ns/yr;
Azimuth measured in degrees, (+) clockwise from north